Journal of Power Sources 196 (2011) 2195–2201

Contents lists available at ScienceDirect

Journal of Power Sources

journal homepage: www.elsevier.com/locate/jpowsour

SnO_2 nanoparticles@polypyrrole nanowires composite as anode materials for rechargeable lithium-ion batteries

Lifeng Cui [a], Jian Shen [a], Fangyi Cheng [a], Zhanliang Tao [a,b,*], Jun Chen [a,b,**]

[a] Institute of New Energy Material Chemistry, Chemistry College, Nankai University, Tianjin 300071, People's Republic of China
[b] Key Laboratory of Advanced Energy Materials Chemistry (Ministry of Education), Chemistry College, Nankai University, Tianjin 300071, People's Republic of China

ARTICLE INFO

Article history:
Received 28 June 2010
Received in revised form 25 August 2010
Accepted 22 September 2010
Available online 1 October 2010

Keywords:
Tin oxide
Polypyrrole
Lithium-ion battery
Nanocomposite
Kinetics

ABSTRACT

The SnO_2@polypyrrole (PPy) nanocomposites have been synthesized by a one-pot oxidative chemical polymerization method. The structure, composition, and morphology of the as-prepared SnO_2@PPy nanocomposites are characterized by XRD, FTIR, TG, SEM, and TEM. Electrochemical investigations show that the obtained SnO_2@PPy nanocomposites exhibit high discharge/charge capacities and favorable cycling when they are employed as anode materials for rechargeable lithium-ion batteries. For the SnO_2@PPy nanocomposite with 79 wt% SnO_2, the electrode reaction kinetics is demonstrated to be controlled by the diffusion of Li^+ ions in the nanocomposite. The calculated diffusion coefficiency of lithium ions in the SnO_2@PPy nanocomposite with 79 wt% SnO_2 is 6.7×10^{-8} cm^2 s^{-1}, while the lithium-alloying activation energy at 0.5 V is 47.3 kJ mol^{-1}, which is obviously lower than that for the bare SnO_2. The enhanced electrode performance with the SnO_2@PPy nanocomposite is proposed to derive from the advantageous nanostructures that allow better structural flexibility, shorter diffusion length, and easier interaction with lithium.

1. Introduction

Rechargeable lithium-ion batteries have been considered as the most prospective power sources for various portable electronic device applications and hybrid electric vehicles [1–3]. Although the graphite anode has shown commercialization, its low theoretical capacity (372 mAh g^{-1}) is insufficient to meet the expanding requirement of higher energy density [4]. Recently, tin oxide-based materials have been proposed as potential substitutive anode for Li-ion batteries due to their high lithium-storage capacity and low potential of lithium alloying/de-alloying [5–7]. However, the main challenge for employing tin oxides as active anode materials is the huge volume variation during lithium–tin (Li–Sn) alloying/de-alloying cycle, which leads to electrode pulverization and rapid capacity decay [8,9].

Up to now, much attention has been paid on improving the cycling performance of tin oxides. Decreasing particle size has been proved as an effective way in moderating the volume change and pulverization of SnO_2 anode [10,11]. Various structures of SnO_2 with small dimensions such as nanowires [12], nanotubes [13], nanoparticles [14], and hollow nanostructures [15] have been synthesized and demonstrated enhanced cycling performance. Especially, one-dimensional (1D) nanostructures (e.g., nanotubes and nanowires) with high length/diameter ratio not only provide more surface reaction sites but also increase the charge-transfer properties of tin-based electrode. For example, the self-catalysis-grown SnO_2 nanowires exhibited reversible capacity over 300 mAh g^{-1} up to 50 cycles and a 15% higher initial coulombic efficiency than that of SnO_2 powder [12].

Moreover, conducting polymers have been investigated as additives to improve the electrode performance because the polymer can provide a conducting backbone for the active materials [16–19]. The soft polymer matrix also shows the function of accommodating the internal stress of anodes that suffer from severe volume change. Thus, the composite with nanosize SnO_2 embedded in conductive polymeric matrix would possess favorable electrochemical properties as anode materials in rechargeable lithium-ion batteries because of coupled structural advantages. In a recent study, SnO_2@polypyrrole (PPy) composites were prepared by first using spray pyrolysis technique to obtain SnO_2 spherical powders and then coating PPy on the surface. After 20 cycles, the composite electrode containing 18.25% PPy retained 70% of its initial capacity (~390 mAh g^{-1}) [19]. However, to the best of our knowledge, a facile synthesis of 1D tin-based polymeric composite nanostructures and their electrochemical study

* Corresponding author at: Institute of New Energy Material Chemistry, Chemistry College, 94 Weijin Road, Nankai University, Tianjin 300071, People's Republic of China. Fax: +86 22 23506808.
** Corresponding author at: Institute of New Energy Material Chemistry, Chemistry College, 94 Weijin Road, Nankai University, Tianjin 300071, People's Republic of China. Tel.: +86 22 23506808; fax: +86 22 23506808.
E-mail addresses: taozhl@nankai.edu.cn (Z. Tao), chenabc@nankai.edu.cn (J. Chen).

0378-7753/$ – see front matter © 2010 Elsevier B.V. All rights reserved.
doi:10.1016/j.jpowsour.2010.09.075

remains uninvestigated. Therefore, we report herein a one-pot in situ chemical-polymerization route to synthesize SnO_2@PPy 1D nanocomposites and the study of their electrode performance. The results show that the as-synthesized SnO_2@PPy nanocomposites display significantly improved cycling performance and enhanced kinetics for Li–Sn alloying in comparison with that of the bare SnO_2 anode.

2. Experimental

2.1. Sample preparation

All reagents were of analytical grade and were purchased from Tianjin chemical reagent company unless otherwise stated. In a typical synthesis, $SnCl_2{\cdot}2H_2O$ (1.3 g) was first dissolved in 100 mL of deionized water containing 5 mL of 30% HCl solution. After stirring for a few minutes, benzene suffocate (0.18 g) was added to the clear solution. Cetyltrimethylammonium bromide (CTAB, 0.3 mmol) was then dissolved to form a homogeneous solution. Pyrrole monomer (0.2 mL, Acros) was added to the above aqueous solution under argon atmosphere. The mixture was stirred vigorously for 15 min at 0–5 °C. Before polymerization, the monomer was distilled and preserved against exposure to light to prevent residual polymerization. Precooled ammonium persulfate (APS) aqueous solution (2.4 g dissolved in 25 mL distilled water) was dripped to the mixture with simultaneous vigorous stirring. The gradual change of color from light black to deep black indicated the formation of PPy. The reaction was maintained under the same conditions for 24 h. Afterwards, the resulting black solid was centrifuged, collected, and washed thoroughly with distilled water and absolute ethanol. Finally, the product was dried at 80 °C for 12 h under vacuum. Similar procedures were carried out to prepare the nanocomposites with different SnO_2 contents. By adjusting the relative amount of pyrrole monomers, SnO_2@PPy nanocomposites with 86, 79, and 67 wt% SnO_2 were prepared and labeled with S2, S3, and S4, respectively. The obtained bare SnO_2 and PPy were denoted as S1 and S5, respectively. The amount of SnO_2 in the as-prepared samples is listed in Table 1.

2.2. Materials characterization

The structures and morphologies of the as-synthesized samples were characterized by powder X-ray diffraction (XRD, Rigaku D/max-2500 X-ray generator, Cu Kα radiation), scanning electron microscopy (SEM, JEOL JSM-6700F Field Emission, 10 kV), and transmission electron microscopy (TEM, Philips Tecnai FEI 20, 200 kV). Infrared spectra of the SnO_2@PPy nanocomposites palletized with KBr were performed on Fourier transformed infrared spectrometer (FTIR, Tianjin Gangdong). To determine the actual amount of polypyrrole in the nanocomposites, thermogravimetric analysis (TGA) was performed using a NETZSCH (TG 209) thermogravimetric analyzer in air atmosphere. The specific surface areas of the samples were analyzed by Brunauer–Emmett–Teller (BET) nitrogen adsorption–desorption measurement (BEL Japan Inc., BELSORP-Mini).

Table 1
Amount of SnO_2 in the as-prepared samples.

Samples	Amount of SnO_2 (wt%)
S1	100
S2	86
S3	79
S4	67
S5	0

2.3. Electrochemical measurements

The working electrode was formulated from a mixture of 80 wt% of SnO_2@PPy nanocomposite, 10 wt% of conducting agent (Cabort, Vulcon XC-72), and 10 wt% of polyvinylidene difluoride (PVDF, Aldrich) binder. The mixture was added to N-methyl-2-pyrrolidinone solvent to form a homogeneous slurry, which was then spread onto a copper foil (⌀ 1.0 cm). This slurry foil was dried in a vacuum oven at 120 °C for 10 h and pressed under an oil machine to make the working electrode with the area of 0.78 cm × 0.78 cm and thickness of 0.1 cm. The amount of SnO_2 in S1, SnO_2@PPy in S2–S4, and PPy in S5 is 1.3, 1.2, 1.1, 1.2, and 1.2 mg, respectively, which is used for the calculation of the electrode capacity. Lithium foil was used as both counter and reference electrodes. The electrolyte comprises 1 M $LiPF_6$ in a 50:50 (w/w) mixture of ethylene carbonate (EC) and diethyl carbonate (DEC). CR2032 coin-type cells were assembled in an argon-filled glove box (Mikrouna Universal 2440/750). All cells were tested galvanostatically at a current density of about 50 mA g^{-1} and were discharged (alloying) and charged (de-alloying) over the potential range of 0.01–2.0 V. The cyclic voltammogram (CV) and electrochemical impedance spectroscopy (EIS) were performed on a Parstat 2273 potentiostat/galvanostat analyzer (Princeton Applied Research & AMETEK Company). The EIS data were collected with an AC voltage of 10 mV amplitude in the frequency range from 1×10^5 to 1×10^{-2} Hz. Prior to EIS measurement, the as-assembled cells were discharged to the requested voltage (0.5 V vs Li^+/Li) and held for 4 h to reach the equilibrium state at 25, 30, 35, 40, and 45 °C, respectively. The EIS results were analyzed by using ZsimpWin software.

3. Results and discussion

3.1. Formation of SnO_2@PPy nanocomposites

The one-pot synthesis of SnO_2@PPy nanocomposites proceeds through in situ oxidation and polymerization process, as shown in Scheme 1. The formation of wire-like polypyrrole nanostructures was achieved by using lamellar inorganic/organic mesostructures as templates [20]. Under the structure-direction effect of surfactant CTAB, pyrrole monomers aggregate to form micelles in aqueous solutions. With dripping ammonium persulfate (APS) solution containing $S_2O_8^{2-}$, Sn^{2+} ions are first oxidized to Sn^{4+} cations, which quickly react with OH^- to form $Sn(OH)_4$ sol. Subsequently, $Sn(OH)_4$ is dispersed in pyrrole micells. When more quantity of APS is added, white $(CTA)_2S_2O_8$ precipitate with lamellar mesostructure is formed, containing pyrrole monomers and $Sn(OH)_4$. In the lamellar $(CTA)_2S_2O_8$, the persulfate anions oxidatively polymerize the pyrrole monomers to polypyrrole. As the formed SO_4^{2-} is dissolved in solution, mesostructural $(CTA)_2S_2O_8$ would degrade, leaving behind the PPy. Meanwhile, excess persulfate anions could diffuse into the vicinity of the degraded $(CTA)_2S_2O_8$ mesostructure, rebuild the mesostructure, and enable any residual pyrrole monomer to be further oxypolymerized at their two edges along the long axes [21]. The subsequent curl and condensation of the lamellar mesostructures results in the well mixed PPy nanowires and $Sn(OH)_4$. After drying, $Sn(OH)_4$ loses water to form crystalline SnO_2 [22], finally producing the SnO_2@PPy nanocomposites.

3.2. Characterization of materials

Fig. 1A shows the XRD patterns of the as-prepared powders. In curve a, all the characteristic diffraction peaks can be assigned to the tetragonal (P42/mnm) structure of SnO_2 (Joint Committee on Powder Diffraction Standards card no. 41-1445). No obvious

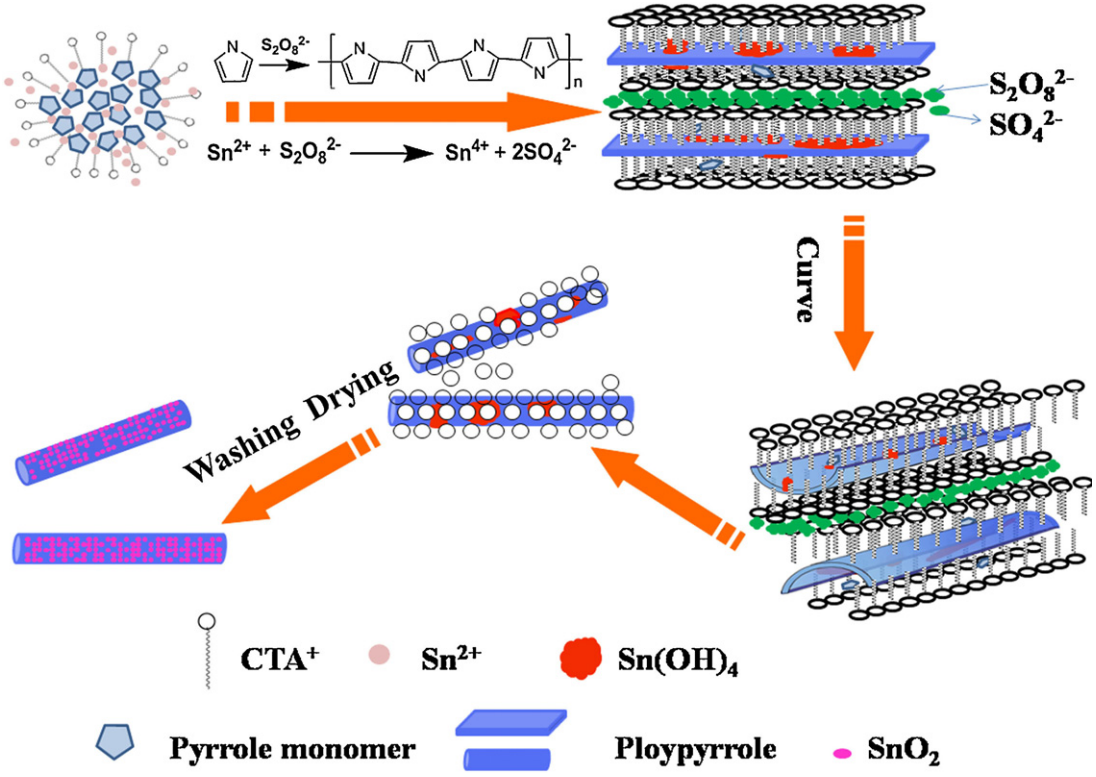

Scheme 1. Schematic illustration of the synthesis of SnO_2@PPy nanocomposites.

peaks corresponding to $SnCl_2$, Sn, or other impurities are observed in the pattern. Broadened peaks are detected in the XRD patterns of the nanocomposites, reflecting their decreased crystallinity and smaller crystallite dimensions. Curve d (S4) displays a broad peak at 22°, which can be attributed to the amorphous PPy phase (data of pure PPy not shown). The mean crystalline sizes calculated by Scherer equation from (1 1 0) plane are 7.7, 3.2, 3.0, and 2.1 nm for sample S1, S2, S3, and S4, respectively.

The FTIR spectra of bare SnO_2 (S1), SnO_2@PPy (S3), and bare PPy (S5) are shown in Fig. 1B. In curves a and b, a strong vibration around 609 cm^{-1} is observed in the low wave number region, which corresponds to antisymmetric Sn–O–Sn mode of the tin oxide. In curves b and c, the band centered at 1560 cm^{-1} corresponds to typical C=C in plane vibration, while the characteristic bands at 1386 and 1205 cm^{-1} are related to C–C and C–H ring stretching, respectively. The sharp peak at 1052 cm^{-1} is attributed to C–H in-plane vibrations. The band at 929 cm^{-1} can be assigned to N–H in-plane

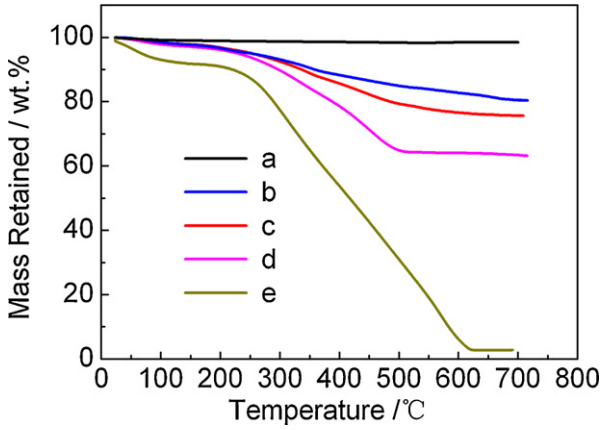

Fig. 2. TGA curves of (a) S1, (b) S2, (c) S3, (d) S4, and (e) S5.

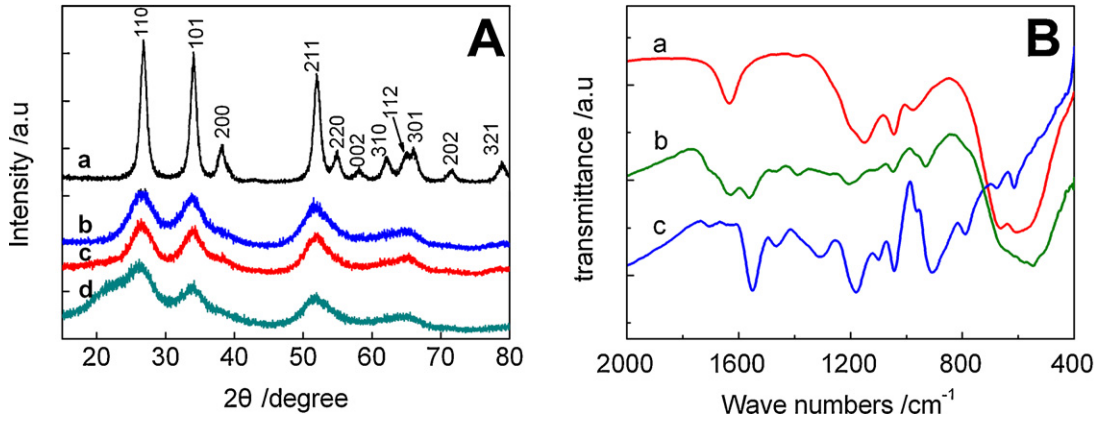

Fig. 1. (A) XRD patterns of the as-prepared products: (a) S1, (b) S2, (c) S3, and (d) S4. (B) FTIR spectra of (a) S1, (b) S3, and (c) S5.

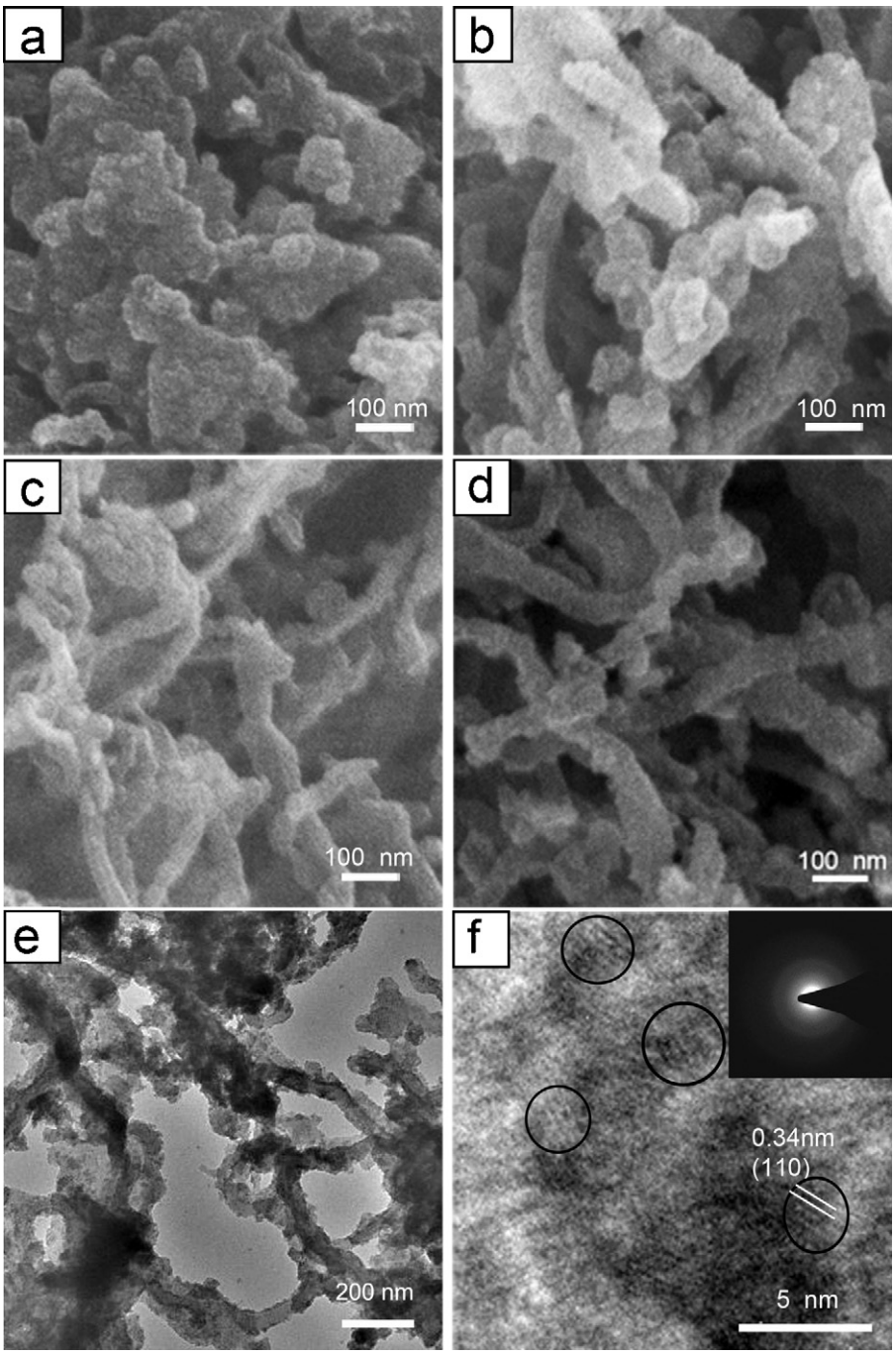

Fig. 3. Typical SEM images of the as-prepared products: (a) S1, (b) S2, (c) S3, and (d) S4. (e) TEM analysis of S3, (f) HRTEM image, and inset: the corresponding SAED pattern taken from (f).

vibrations [23,24]. Therefore, FTIR results ascertain the presence of PPy in the as-prepared SnO_2@PPy nanocomposite.

For quantifying the amount of PPy in the as-synthesized SnO_2@PPy composite samples, thermogravimetric analysis was carried out in air atmosphere (Fig. 2). The samples were heated from 25 to 700 °C at a rate of 10 °C min^{-1}, displaying two weight loss regions. The first weight loss in the temperature range of 25–250 °C is attributed to the desorption of physisorbed water, while the second in the range of 250–700 °C is ascribed to the oxidation of PPy [25]. The bare SnO_2 (S1) shows almost no weight change in the whole investigated temperature range. In comparison, the pure PPy sample (S5) is burnt off. Therefore, according to the change in weight before and after the oxidation of PPy, the content of SnO_2 in the nanocomposites can be calculated, which is 86 wt%, 79 wt%, and 67 wt% for the synthesized samples S2, S3, and S4, respectively.

Fig. 3 shows the morphologies of the as-prepared products. Pure SnO_2 sample (S1) is composed of agglomerate particles with average diameter of more than 200 nm (Fig. 3a). Some nanowires emerge in the SnO_2@PPy composite with 14 wt% PPy (S2), as shown in the typical SEM image in Fig. 3b. When the PPy amount in the nanocomposite is further increased, long, interlaced, and wirelike structures can be clearly observed (Fig. 3c and d). The representative TEM image (Fig. 3e) of the as-prepared S3 (containing 21 wt% PPy) reveals that the length of the composite wires is in the range of 1–2 μm while the average diameter is approximately 60 nm. In addition, the SnO_2 nanoparticles are homogeneously distributed in

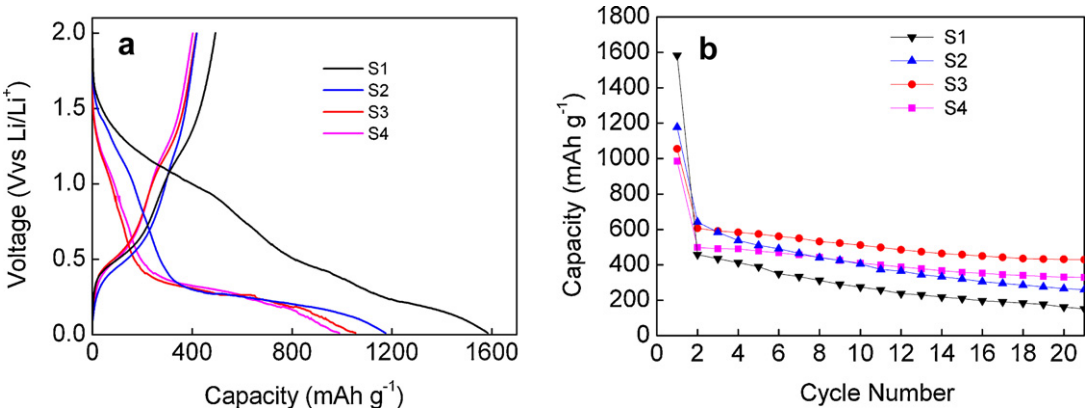

Fig. 4. (a) The discharge/charge curves in the first cycle and (b) cycling performance of bare SnO_2 and SnO_2@PPy nanocomposites. The voltage window is set between 0.1 and 2 V and the current density is 50 mA g^{-1}.

the PPy matrix. Furthermore, the HRTEM image in Fig. 3f shows lattice fringes, indicating that the marked SnO_2 nanoparticles are polycrystalline. The corresponding selected area electron diffraction (SAED) pattern (inset) also corroborates the polycrystallinity of the synthesized nanocomposite, which is in agreement with the XRD analysis.

3.3. Electrochemical properties

3.3.1. Charge/discharge curves and cycling performance

The as-synthesized bare SnO_2 and SnO_2@PPy nanocomposites were employed as active materials to assemble laboratory lithium-ion cells. Fig. 4a shows the typical galvanostatic charge and discharge profiles. The initial discharge capacities are 1583, 1177, 1055, and 985 mAh g^{-1} for S1, S2, S3, and S4, respectively. The initial discharge capacity of pure PPy (S5) is only 1.2 mAh g^{-1}, which is not detected later. The charge capacities of S1, S2, S3, and S4 in the first cycle are 493, 417, 416, and 401 mAh g^{-1}, respectively. These large capacity losses between the discharge and charge in the first cycle are attributed to the formation of Li_2O and solid-electrolyte interface (SEI) during the first charge/discharge process [26]. After 20 cycles (Fig. 4b), the capacities of S1, S2, S3, and S4 are 152, 260, 430, and 330 mAh g^{-1}, which correspond to 10.3%, 22.5%, 40.8%, and 33.5% retention of their initial capacities. Therefore, SnO_2@PPy nanocomposites show improved cyclability to the bare SnO_2. Since the as-prepared PPy does not contribute to the capacity, illustrating that it is taking the role of conducting the SnO_2 due to their highly dispersion. This nanocomposite structure favors the release

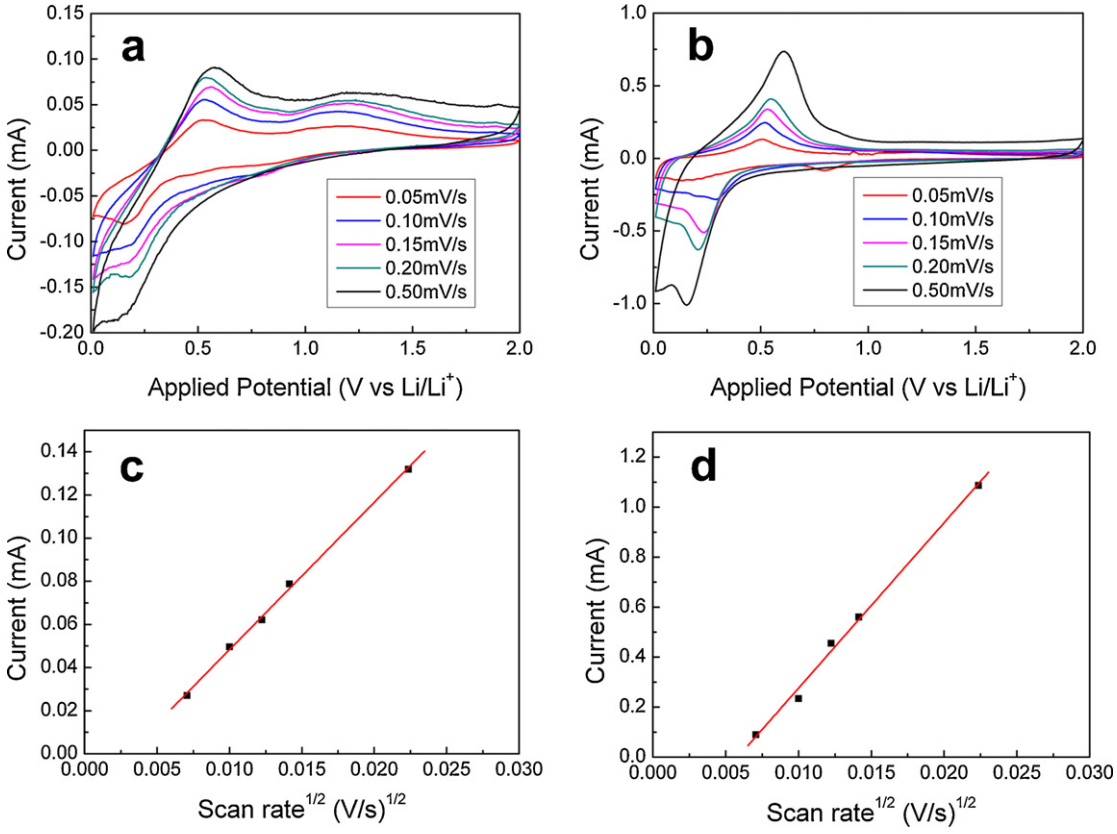

Fig. 5. Cyclic voltammograms of (a) S1 and (b) S3 composite. The scan rates are 0.05, 0.1, 0.15, 0.2, and 0.5 mV s^{-1}, respectively. Plots of peak current (I_p) as a function of the square root of the scan rates ($v^{1/2}$) for (c) S1 and (d) S3 composite.

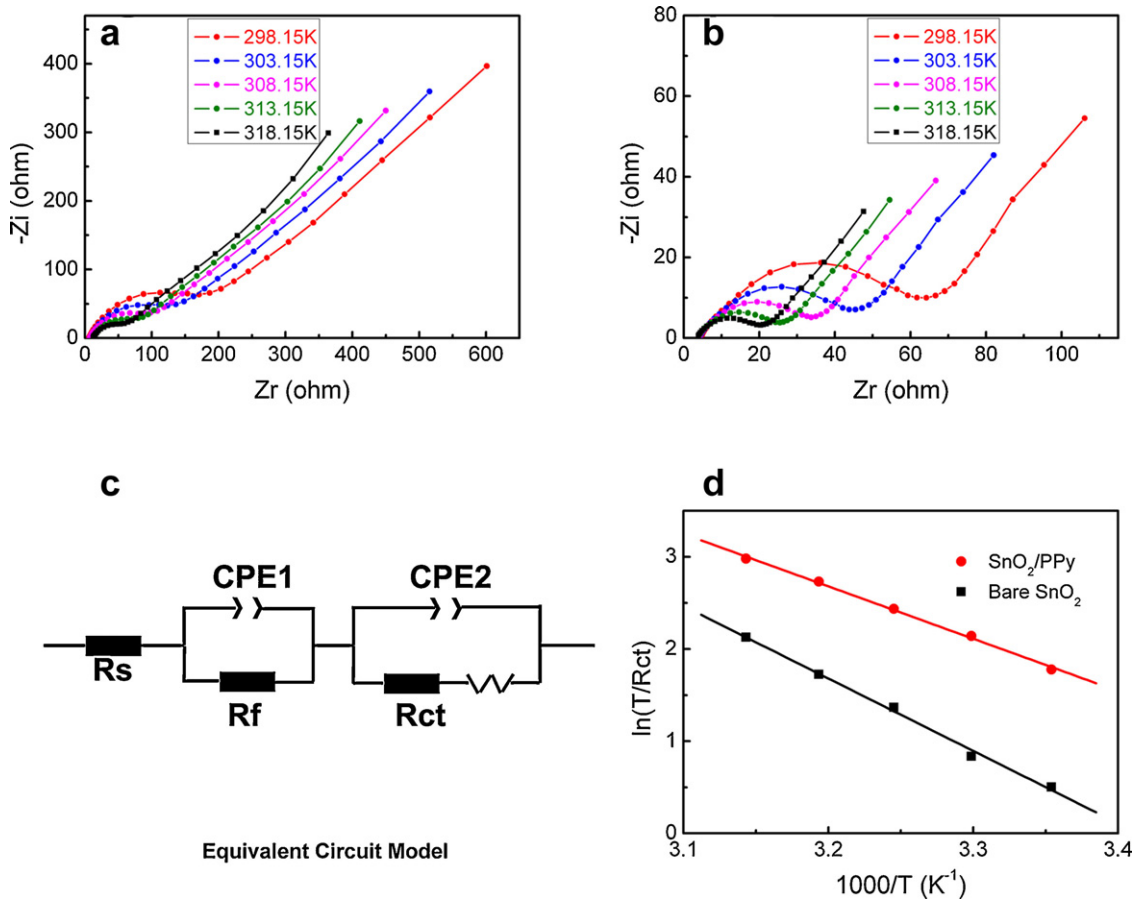

Fig. 6. Electrochemical impedance spectra (EIS) for the cells made of (a) S1 and (b) S3 at 0.5 V. (c) The corresponding equivalent circuit. (d) Arrhenius plots of $\ln(T/R_{ct})$ vs $1/T$.

of the stress caused by the drastic volume variation during the Li–Sn alloying/de-alloying process, and improves the utilization of active SnO_2.

In our examined data, it is noted that the as-prepared SnO_2@PPy nanocomposite containing 79 wt% SnO_2 (S3) exhibits the best cycling performance. The capacity (430 mAh g^{-1}) of S3 after 20 cycles is nearly 3 times that of the bare SnO_2. This result shows that the promising addition of PPy in SnO_2 is around 20% in weight. The improved capacity and cyclability of S3 prompt us to further investigate the electrode kinetics in comparison of S1. The specific surface areas of S1 and S3 estimated from the Brunauer–Emmett–Teller (BET) method are 5.6 and 7.3 $m^2\,g^{-1}$, respectively. Barrett–Joyner–Halenda (BJH) analysis shows that S3 displays a pore size distribution between 3 and 20 nm, while S1 gives a narrow pore size distribution only around 15 nm.

3.3.2. Diffusion coefficiency

Cyclic voltammetry analysis has been carried out to understand the improved electrochemical characteristics of SnO_2@PPy nanocomposites. Fig. 5a and b displays the cyclic voltammograms (CVs) of the comparative bare SnO_2 electrode and the SnO_2@PPy nanocomposite (S3), respectively. At the same potential sweep rates, the nanocomposite shows significantly higher peak current density than that of bare SnO_2, indicating the obviously enhanced reactivity of the nanocomposite. By using CVs, the kinetic response is examined to determine the dependence of peak currents (I_p) on scan rates (v). The diffusion coefficient of Li^+ ions (D_{Li}) can be calculated from a linear relationship between I_p and $v^{1/2}$ according to the following equation [27,28]:

$$I_p = 2.69 \times 10^5 n^{3/2} A D_{Li}^{1/2} C_{Li}^* v^{1/2} \quad (1)$$

where n is the number of electrons per reaction species (it is 1 for Li^+), A is the electrode area (cm^2), and C_{Li}^* is the bulk concentration of the Li^+ ion in the electrode (mol cm^{-3}). Fig. 5c and d shows a good linear relationship between I_p and $v^{1/2}$ for both S1 and S3. The Li^+ diffusion coefficiency in the SnO_2@PPy nanocomposite (S3) is calculated to be 6.7×10^{-8} $cm^2\,s^{-1}$. In comparison, the diffusion coefficiency for the bare SnO_2 (S1) shows a lower value of 7.2×10^{-10} $cm^2\,s^{-1}$. This result indicates that the transportation rates of Li^+ in SnO_2@PPy nanocomposites are about two orders higher than that in bare SnO_2. This enhancement could be attributed to the unique structure and morphology of SnO_2@PPy nanocomposite, in which the porous and conductive PPy matrix serves as efficient diffusion channels for Li^+.

3.3.3. Activation energies

To further investigate the electrode kinetics, the activation energies of the nanocomposite and bare SnO_2 are calculated from EIS data with a previously reported method [29,30]. Fig. 6a and b shows the EIS analyses of the electrodes of S1 and S3 at 0.5 V. It can be observed that the impedance curves consist of one compressed semicircle in the medium-frequency region and an inclined line in the low-frequency region. The impedance plots were fitted by using the equivalent circuit model (Fig. 6c), which includes the electrolyte resistance R_s, the SEI resistance R_f, the charge-transfer resistance R_{ct}, the Warburg impedance (Z_w) related to the diffusion of lithium ions into the bulk of the electrode materials, and two constant phase elements (CPE1 and CPE2) associated with the interfacial resistance and charge-transfer resistance, respectively. The intercept of the impedance semicircle at high frequency region corresponds to R_s in the equivalent circuit. Although barely observ-

Table 2
Charge-transfer resistance (R_{ct}), exchange current (i_0), and apparent activation energies (E_a) of the electrodes with bare SnO_2 (S1) and SnO_2@PPy composite (S3) measured at different temperatures.

Sample	R_{ct} (Ω)					i_0 (mA)					Apparent activation energy (kJ mol^{-1})
	25 °C	30 °C	35 °C	40 °C	45 °C	25 °C	30 °C	35 °C	40 °C	45 °C	
S1	180.4	131.4	78.5	55.8	37.8	0.142	0.199	0.338	0.484	0.725	65.3
S3	50.4	35.6	27.0	20.4	16.2	0.510	0.734	0.983	1.323	1.692	47.3

able in Fig. 6a and b, R_s values do change with temperature. For example, when the temperature was raised from 298 K to 318 K, R_s of S3 decreased from 5.1 Ω to 4.1 Ω. Such change, however, is negligible in comparison with the change of R_{ct}. Table 2 summarizes the fitted EIS results. Obviously, the R_{ct} of the SnO_2@PPy composite is significantly smaller than that of the bare SnO_2, suggesting that the electrode conductivity can be greatly increased by PPy-compositing.

The exchange currents (i_0) and the apparent activation energies for the alloying of lithium can be calculated by Eq. (2) and the Arrhenius equation (Eq. (3)), respectively:

$$i_0 = \frac{RT}{nFR_{ct}} \tag{2}$$

$$i_0 = A \exp\left(\frac{-E_a}{RT}\right) \tag{3}$$

where A is a temperature-independent coefficient, R is the gas constant, T is the absolute temperature, n is the number of transferred electrons, and F is the Faraday constant. The following equation can be deduced from Eqs. (2) and (3):

$$\ln\frac{T}{R_{ct}} = \ln\frac{nFA}{R} - \frac{E_a}{RT} \tag{4}$$

According to the above equation, the apparent activation energies were obtained by calculating the slope of the plot of $\ln(T/R_{ct})$ as a function of 1000/T. The determined value for the SnO_2@PPy composite (S3) is 47.3 kJ mol^{-1}, which is much lower than that (65.3 kJ mol^{-1}) for bare SnO_2 (S1). The lower activation energies of SnO_2@PPy composite indicate facilitated lithium–tin alloying. This enhanced electrode kinetics is probably due to the fact that the 1D nanostructures provide shorter diffusion route for Li^+, and that the flexible PPy substrate can efficiently disperse the supported and embedded SnO_2 nanoparticles to alleviate the aggregation of the formed tin small particles and to accommodate the strain generated during the process of lithium insertion/extraction.

4. Conclusions

In summary, SnO_2@PPy nanocomposites have been prepared via a simple in situ oxidative chemical polymerization approach at near room temperature. The as-prepared nanocomposites as anode materials for lithium-ion batteries show enhanced electrode performance for Li–Sn alloying/de-alloying. The reason is that the SnO_2@PPy nanocomposites exhibit remarkably higher Li^+ diffusion coefficiency and much lower activation energy than that of bare SnO_2 electrode. The enhanced charge/discharge cyclability and electrode kinetics are ascribed to the 1D nanostructures and highly dispersion of SnO_2 nanoparticles in PPy matrix, which are beneficial to the utilization of active SnO_2 owing to the release of the stress caused by the drastic volume variation during the Li–Sn alloying/de-alloying process.

Acknowledgements

This study was supported by the Research Programs of National NSFC (20703026), MOE (IRT0927), Tianjin Basic and High-Tech Development (07ZCGHHZ00700 and 08JCZDJC21300).

References

[1] J.M. Tarascon, M. Armand, Nature 414 (2001) 359–367.
[2] J. Chen, F.Y. Cheng, Acc. Chem. Res. 42 (2009) 713–723.
[3] J.O. Besenhard, J. Yang, M. Winter, J. Power Sources 68 (1997) 87–90.
[4] J. Read, D. Foster, J. Wolfenstine, W. Behl, J. Power Sources 96 (2001) 277–281.
[5] M. Winter, J.O. Besenhard, Electrochim. Acta 45 (1999) 31–50.
[6] I.A. Courtney, J.R. Dahn, J. Electrochem. Soc. 144 (1997) 2943–2948.
[7] F.Y. Cheng, Z.L. Tao, J. Liang, J. Chen, Chem. Mater. 20 (2008) 667–681.
[8] Y.N. Nuli, S.L. Zhao, Q.Z. Qin, J. Power Sources 114 (2003) 113–120.
[9] X.W. Lou, D. Deng, J.Y. Lee, L.A. Archer, Chem. Mater. 20 (2008) 6562–6566.
[10] Y.D. Wang, I. Djerdj, B. Smarsly, M. Antonietti, Chem. Mater. 21 (2009) 3202–3209.
[11] Y. Wang, J.Y. Lee, J. Power Sources 144 (2005) 220–225.
[12] M.S. Park, G.X. Wang, Y.M. Kang, D. Wexler, S.X. Dou, H.K. Liu, Angew. Chem. Int. 46 (2007) 750–753.
[13] Y. Wang, J.Y. Lee, H.C. Zeng, Chem. Mater. 17 (2005) 3899–3903.
[14] A. Sivashanmugam, T.P. Kumar, N.G. Renganathan, S. Gopukumar, M. Wohlfahrt-Mehrens, J. Garche, J. Power Sources 144 (2005) 197–203.
[15] X.W. Lou, Y. Wang, C.L. Yuan, J.Y. Lee, L.A. Archer, Adv. Mater. 18 (2006) 2325.
[16] A. Du Pasquier, F. Orsini, A.S. Gozdz, J.M. Tarascon, J. Power Sources 82 (1999) 607–611.
[17] B. Veeraraghavan, J. Paul, B. Haran, B. Popov, J. Power Sources 109 (2002) 377–387.
[18] G.X. Wang, L. Yang, Y. Chen, J.Z. Wang, S. Bewlay, H.K. Liu, Electrochim. Acta 50 (2005) 4649–4654.
[19] L. Yuan, J. Wang, S.Y. Chew, J. Chen, Z.P. Guo, L. Zhao, K. Konstantinov, H.K. Liu, J. Power Sources 174 (2007) 1183–1187.
[20] X.T. Zhang, J. Zhang, Z.F. Liu, C. Robinson, Chem. Commun. (2004) 1852–1853.
[21] Y.D. Li, X.L. Li, Z.X. Deng, B.C. Zhou, S.S. Fan, J.W. Wang, X.M. Sun, Angew. Chem. Int. 41 (2002) 333–335.
[22] A. Sivashanmugam, T. Premkumar, S. Gopukumar, N.G. Renganathan, M. Wohlfahrt-Mehrens, J. Garche, J. Appl. Electrochem. 35 (2005) 1045–1050.
[23] G.J. Cho, B.M. Fung, D.T. Glatzhofer, J.S. Lee, Y.G. Shul, Langmuir 17 (2001) 456–461.
[24] J.W. Liu, J.X. Qiu, Y.Q. Miao, J.R. Chen, J. Mater. Sci. 43 (2008) 6285–6288.
[25] S.V. Vasilyeva, M.A. Vorotyntsev, I. Bezverkhyy, E. Lesniewska, O. Heintz, R. Chassagnon, J. Phys. Chem. C 112 (2008) 19878–19885.
[26] I.A. Courtney, J.R. Dahn, J. Electrochem. Soc. 144 (1997) 2045–2052.
[27] A.J. Bard, L.R. Faulkner, Electrochemical Methods: Fundamentals and Applications, second ed., John Wiley, 2000.
[28] T. Zhang, L.J. Fu, J. Gao, Y.P. Wu, R. Holze, H.Q. Wu, J. Power Sources 174 (2007) 770–773.
[29] S.L. Chou, J.Z. Wang, H.K. Liu, S.X. Dou, Electrochem. Commun. 11 (2009) 242–246.
[30] H. Ma, S.Y. Zhang, W.Q. Ji, Z.L. Tao, J. Chen, J. Am. Chem. Soc. 130 (2008) 5361–5367.